Title
Variations in the amount of water ice on Ceres' surface suggest a seasonal water cycle.

Journal
Science advances, 4(3)

ISSN
2375-2548

Authors
Raponi, Andrea
De Sanctis, Maria Cristina
Frigeri, Alessandro
et al.

Publication Date
2018-03-01

DOI
10.1126/sciadv.aao3757

Peer reviewed

SPACE SCIENCES

Variations in the amount of water ice on Ceres' surface suggest a seasonal water cycle

Andrea Raponi,[1]* Maria Cristina De Sanctis,[1] Alessandro Frigeri,[1] Eleonora Ammannito,[2] Mauro Ciarniello,[1] Michelangelo Formisano,[1] Jean-Philippe Combe,[3] Gianfranco Magni,[1] Federico Tosi,[1] Filippo Giacomo Carrozzo,[1] Sergio Fonte,[1] Marco Giardino,[1] Steven P. Joy,[4] Carol A. Polanskey,[5] Marc D. Rayman,[5] Fabrizio Capaccioni,[1] Maria Teresa Capria,[1] Andrea Longobardo,[1] Ernesto Palomba,[1] Francesca Zambon,[1] Carol A. Raymond,[5] Christopher T. Russell[4]

The dwarf planet Ceres is known to host a considerable amount of water in its interior, and areas of water ice were detected by the Dawn spacecraft on its surface. Moreover, sporadic water and hydroxyl emissions have been observed from space telescopes. We report the detection of water ice in a mid-latitude crater and its unexpected variation with time. The Dawn spectrometer data show a change of water ice signatures over a period of 6 months, which is well modeled as ~2-km^2 increase of water ice. The observed increase, coupled with Ceres' orbital parameters, points to an ongoing process that seems correlated with solar flux. The reported variation on Ceres' surface indicates that this body is chemically and physically active at the present time.

INTRODUCTION

Ceres contains significant amounts of water (*1*), which is a key element of its evolution (*2*), composition (*3*), and activity (*2*). Water ice has been estimated to be ubiquitous and abundant within a few meters from the surface (*4*). Exposed water ice was also discovered by the Dawn mission in a few craters on Ceres situated in the northern hemisphere above 42° latitude, indicating a strong dependence of water ice stability with the surface illumination condition and temperatures (*5*, *6*). A notable exception is represented by Juling crater (Fig. 1A), being situated in a mid-latitude, in the southern hemisphere (35°S, 168°E), where the Dawn visible and infrared (VIR) mapping spectrometer (*7*) detected water ice owing to the diagnostic absorption bands at 1.25, 1.5, 2.0, and 3.0 μm (Fig. 1B). VIR detected ice on the northern shadowed crater wall, characterized by an almost vertical rocky cliff, illuminated by a secondary light source coming from the adjacent illuminated regions. The crater floor shows evidence of the flow of ice and rock, similar to Earth's rock glacier (fig. S1) (*8*).

This crater has been observed by VIR several times: two times with a nominal spatial resolution of ~100 m per pixel during the Low Altitude Mapping Orbit (L1 and L2) and three times with a nominal spatial resolution of ~400 m per pixel during a phase devoted to Juling's observation: Extended Juling Orbit (E1, E2, and E3).

RESULTS

Analyzing all the acquisitions, we discovered changes in the spectra of the ice-rich wall. Water bands were detected in all the observations on the northern wall of Juling but with a variation of the water ice features, in particular, the 2.0-μm water ice absorption (Fig. 2) that is the most prominent band and least affected by instrumental errors.

However, the rim and wall were observed under different conditions in terms of (i) illumination and viewing geometry (table S1) and (ii) sampling and resolution. Because these conditions might affect the spectral shape, we accounted for them as follows:

1) We noticed that illumination and viewing geometry can be considered equal in E1 and L1 (table S1), thus permitting a direct comparison of the measured spectra (Fig. 3). All the other observations have been compared by means of dedicated modeling, as discussed afterward.

2) The different spatial resolution and different sampling of the surface by the observations (fig. S2) are taken into account calculating an average spectrum, obtained over several pixels in the target area (see the Supplementary Materials). The selected area is defined by a rectangle of coordinates in latitude = [−35.0643, −34.7051] and longitude = [167.8362, 169.1599] (Fig. 3). The rectangle was chosen to be larger than the area containing the ice-rich wall, to include all pixels showing water ice signatures, considering the extension of the instrument point spread function (fig. S3). The resulting average spectra are shown in Fig. 2A.

The spectra shown in Fig. 2 are affected by different illumination conditions and viewing geometry, and they cannot be compared directly to infer intrinsic water ice variation. However, these conditions are very similar for L1 and E1 observations, allowing a direct comparison. The direct comparison between L1 and E1 shows significant differences, with more pronounced ice spectral signatures in E1 (Figs. 2 and 3). We verified this approach by comparing the spectra of a test area without ice signatures. In this case, no significant variation in the spectra can be detected, ruling out any bias due to the different spatial resolution and sampling as well as illumination conditions (Fig. 3).

The selected ice-rich area (Fig. 3) includes both the signal coming from the wall, indirectly illuminated by the light reflected by the crater floor, and the signal coming from a region outside the crater rim, directly illuminated by the Sun. By modeling the average spectra as the sum of the two contributions (fig. S4), we estimate the spectrum of the ice-rich wall and its band area at 2.0 μm for all observations (L1, L2, E1, E2, and E3), as explained in the Supplementary Materials.

[1]Istituto di Astrofisica e Planetologia Spaziali, INAF, Via del Fosso del Cavaliere 100, 00133 Roma, Italy. [2]Agenzia Spaziale Italiana, Via del Politecnico, 00133 Roma, Italy. [3]Bear Fight Institute, 22 Fiddler's Road, P.O. Box 667, Winthrop, WA 98862, USA. [4]Institute of Geophysics and Planetary Physics, University of California, Los Angeles, 603 Charles E. Young Drive, East, Los Angeles, CA 90095, USA. [5]NASA/Jet Propulsion Laboratory, California Institute of Technology, 4800 Oak Grove Drive, Pasadena, CA 91109, USA.
*Corresponding author. Email: andrea.raponi@iaps.inaf.it

Using this approach, we can compare all the observations. Figure 4A shows a clear increase of the derived 2.0-μm band area from ice-rich wall as a function of time.

Intrinsic variations of the band area can be attributed to changing abundances of water ice, as well as other physical properties, such as changes in grain size. Using the model described in Materials and Methods, the spectra can be modeled by an areal mixture of regolith and water ice, and the observed variation of spectral signatures can be explained by an increasing abundance of water ice as a function of time, with an effective grain diameter fixed to 100 μm (see fig. S5). Best fits of the spectra are shown in fig. S6. As a further check, considering the information on the illumination condition and viewing geometry, we simulated the spectra of all observations assuming a constant ice abundance. The simulations show that a constant quantity of water ice is incompatible with the observations (fig. S7).

According to the modeled spectra, the total area of the ice-rich wall results to be covered by 9.1 ± 0.3% of water ice in the first observation and by 13.7 ± 0.9% of water ice in the last observation (Fig. 4A and table S2). Using shape model analysis, we estimated the total surface of the wall to be ~40 km^2, from which we obtain an increase from 3.6 to 5.5 km^2 (±0.4 km^2) of the surface covered by water ice.

DISCUSSION

The observed increasing abundance of water ice on the crater wall implies a change in temperature/pressure induced by (i) internal processes, (ii) exposure of ice present behind a regolith layer by falls, or (iii) solar input.

i) One possible internal process would involve subsurface displacement of brine or liquid water, which, percolating through clay layers, freezes when exposed to the shadowed cold surface of the wall. The flow features on the crater floor would favor this hypothesis, but this scenario is difficult to reconcile with current evolution models of Ceres' interior (*2*). Water in liquid or brine forms would imply either higher internal

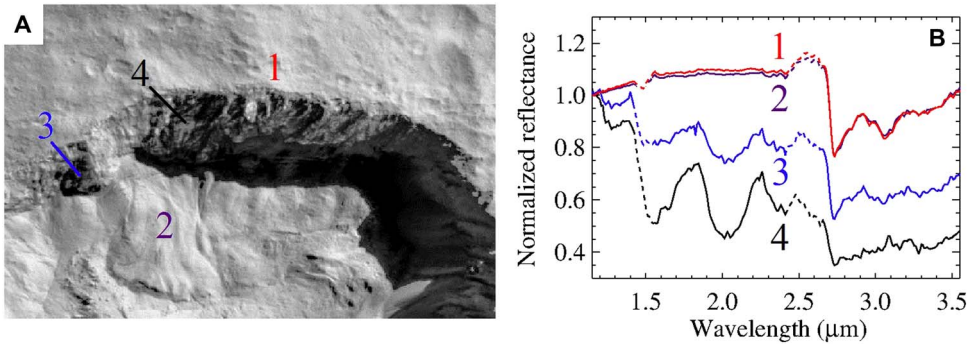

Fig. 1. General context of the ice-rich area in Juling crater from Framing Camera and VIR spectrometer data. (**A**) Context Dawn Framing Camera image taken during L1 acquisition of the northern rim of Juling crater. The area in shadow is enhanced to show details of the ice-rich wall. (**B**) Measured spectra corresponding to positions in (A). Dotted lines represent spectra in the ranges corresponding to instrument filter junctions that could produce fictitious signals. The diagnostic absorption bands of water ice at 1.25, 1.5, and 2.0 μm are visible. The broad absorption band of water ice at 3.0 μm is superimposed to the narrower absorption bands at 2.7, 3.1, and 3.4 μm, which indicates the presence of Mg phyllosilicates, NH_4 phyllosilicates, and Mg carbonates (*3*), respectively. These minerals are ubiquitous on Ceres' surface (*3*).

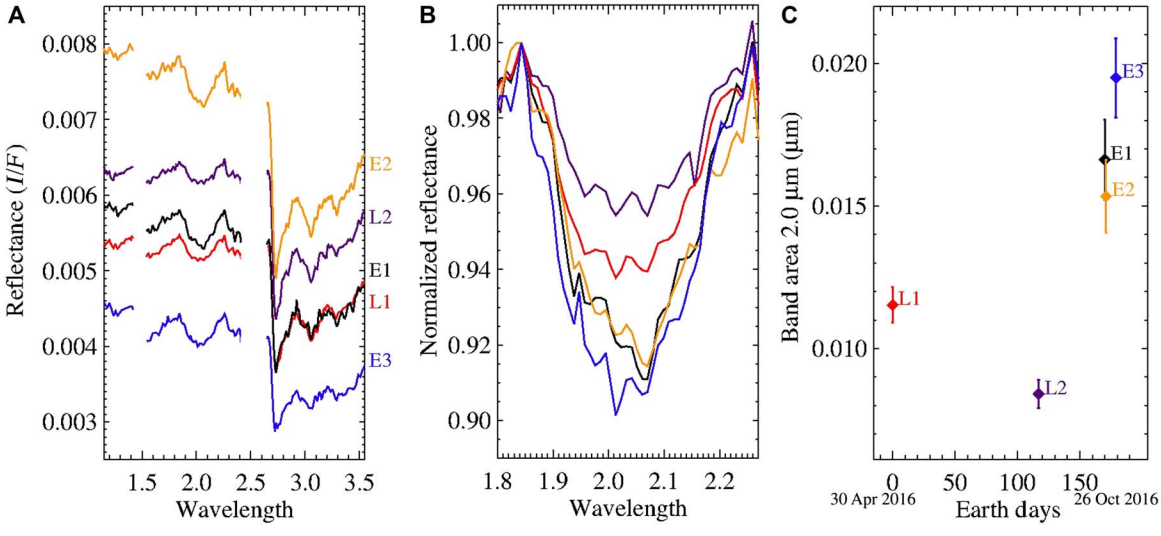

Fig. 2. Measured average spectra and their band area at 2.0 μm from the ice-rich region. (**A**) Average spectra for each of the five observations from pixels in the rectangle of coordinates: latitude = [−35.0643, −34.7051] and longitude = [167.8362, 169.1599]. Spectral ranges corresponding to the instrument filter junctions are not shown. (**B**) Absorption band at 2.0 μm normalized at 1.83 μm. (**C**) Band area measured as a function of Earth days by setting the day of the first observation (L1) equal to 0.

temperatures with respect to those foreseen for Ceres or much lower melting point (*9*). Nevertheless, subsurface brines have been suggested to explain the morphology and composition of the Occator central dome (*9*), and cryovolcanism has been indicated as the source of Ahuna Mons (*10*). Moreover, Ceres topography suggests the presence of liquid pore fluids in the uppermost mantle (*11*).

ii) Another possibility is represented by falls exposing water ice. The monotonic trend (Fig. 4A) is not consistent with an exceptional event, such as a rock fall exposing water ice. However, a continuous erosion of the wall by regolith falls is possible, and it can justify the formation of the rock glaciers. In that case, the increase of ice on the wall can be explained by the exposure of pristine water ice, which does not sublimate with the same rate of its exposure during the season of the observations.

iii) Other mechanisms would involve water vapor, which has been observed by Küppers *et al.* (*12*) and A'Hearn and Feldman (*13*). Water vapor might originate from the rock glaciers on the crater floor below a regolith layer, and the shadowed wall of the crater may be a cold trap for the water molecules. As long as the accumulation rate of water molecules is higher than the sublimation rate from the wall itself, the ice on the wall increases. Considering the derived 1.9-km^2 (±0.4 km^2) increase of ice cross section and assuming a grain diameter of 100 μm, we obtain an increase of the volume of water ice of 125 ± 25 m^3 in 6 months. The equivalent average accumulation rate (net of sublimation) is 8.0 ± 1.6 g/s (ρ_{H_2O} = 1 g/cm^3).

It has been suggested that the observed water vapor (*12*) was triggered by solar radiation (*12*) and/or solar energetic particle events (*14*). The changes in heliocentric distance (Fig. 4 and table S1), coupled

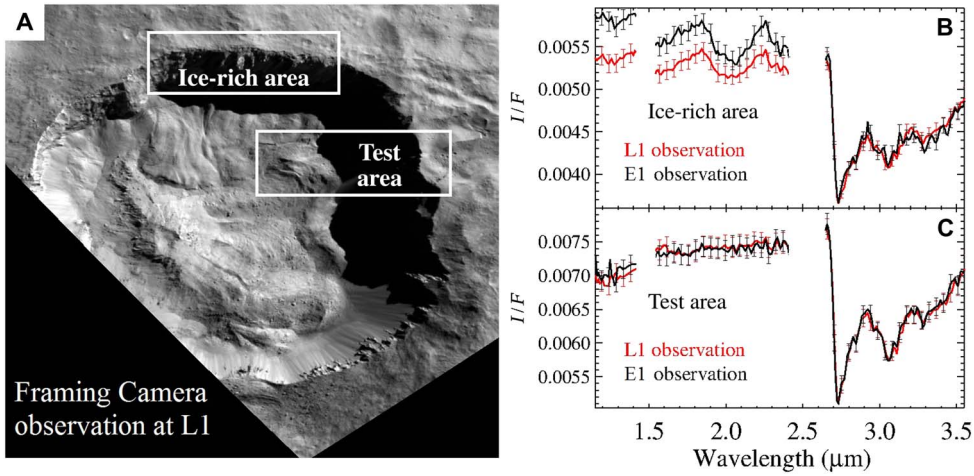

Fig. 3. Comparison of L1 and E1 observations in the ice-rich area and in a test area. (**A**) Average spectra of pixels in the rectangle (latitude = [35.0643, −34.7051]; longitude = [167.8362, 169.1599]) are used as a reference to compare the five observations. Two measured spectra from L1 and E1 can be directly compared due to the equal viewing geometry and illumination conditions. (**B**) The increase of water ice signatures and continuum level is clearly visible. Error bars include Poissonian noise and calibration uncertainty. (**C**) Comparison of average spectra from a test area (latitude = [−35.714045, −35.292928]; longitude = [168.6245, 169.8397]) does not show any significant variation.

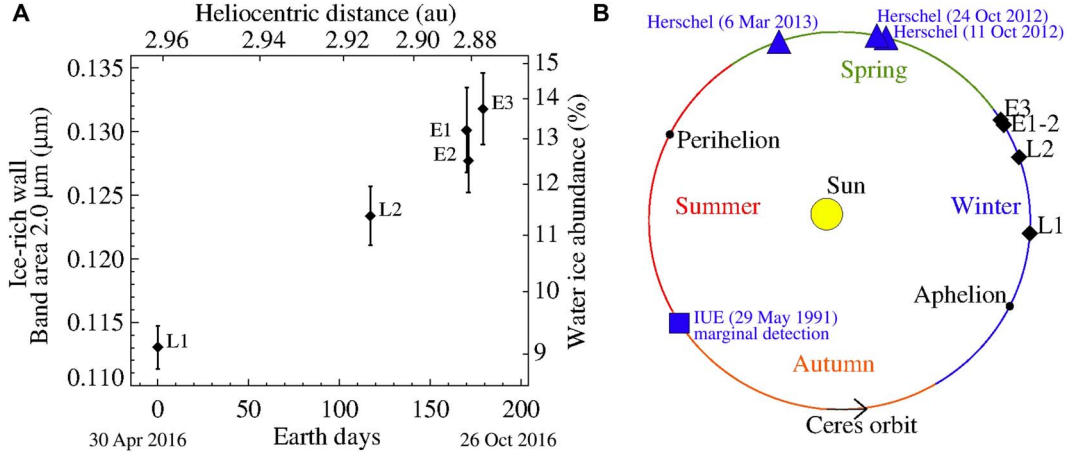

Fig. 4. Modeled increase of water ice on the crater wall and contextualization along Ceres' orbit. (**A**) Left axis: Band area at 2.0 μm calculated after isolation of the signal of the ice-rich wall by removal of the outer signal from average spectrum. Right axis: Water ice abundance as retrieved by the model (table S2). Both quantities are shown as a function of Earth days by setting the day of the first observation (L1) equal to 0. Error bars are estimated as discussed in the Supplementary Materials. au, astronomical unit. (**B**) Ceres orbit with International Ultraviolet Explorer (IUE) and Herschel water detections (*12*, *13*). The orbit segment associated with the Juling observations indicates an increasing solar flux in the southern hemisphere of Ceres, where Juling is located.

with the varying season (the subsolar point was moving toward lower latitudes), result in a net increase in solar flux and a retreat of shadow on the floor (fig. S8). We used a thermophysical model to simulate the water flux coming from the crater floor, triggered by solar radiation, at the epoch of Herschel observations (*15*, *16*). Assuming that the crater floor is filled by water ice at ~1 cm below the surface, the estimated vapor flux coming from the crater is comparable to the total flux derived from Herschel observations (fig. S9). Moreover, Juling is located in proximity of the longitudinal coordinate, where the maximum emission was observed by Küppers *et al.* (*12*). However, we do not have constraints to derive the extension of the ice layer and the thickness of the superficial regolith layer. Thus, if water ice is confined below the thermal skin depth, then the solar radiation would not be sufficient to sublimate enough water vapor.

Solar energetic protons have been indicated as possible sources of water vapor (*14*) because they could reach ice present in deeper subsurficial layers. Although these also might affect the surface ice at Juling, the event observed by Dawn (*14*) lasted about a day and the ensuing exosphere remained for a week. Hence, any lost water from Juling's cold shadowed walls could be replenished.

The linear relationship between ice abundance and solar flux (fig. S8) supports the possibility of solar flux as the main factor responsible for the observed increase. The water ice abundance on the wall is probably not constantly increasing over a longer time range. More likely, we are observing only part of a seasonal cycle of water sublimation and condensation, in which the observed increase should be followed by a decrease. Similar cycles of water ice have been observed for comet 67P/C-G (*17*–*20*) related to changes in heat flux.

The orbital parameters of Ceres could justify such a cyclical trend (see Fig. 4B). After the period covered by the observations, Ceres approaches the summer solstice, close to perihelion, where the temperature of the shadowed area increases, possibly triggering also the sublimation of water ice previously accumulated on the cold wall or sublimating pristine water ice with higher rate than its exposure.

The variation of superficial water ice occurring in the short time frame covered by these observations provides new scenarios for Ceres' evolution. It indicates an active body and reinforces not only the link with the icy solar system objects (*3*) but also the uniqueness of Ceres, given its present location in the main belt.

MATERIALS AND METHODS

Non-intrinsic sources of spectral variability among different observations

To correctly compare the average spectra measured for the five observations of the ice-rich wall of Juling crater, we should take into account the non-intrinsic sources of spectral variability due to different conditions of observation:

1) Poissonian noise, which produces spurious spectral variability among different measured spectra. This noise is less significant for average spectra obtained by a large number of measurements. It minimizes the noise for the average spectra analyzed in the present work because the average spectra are derived from tens or hundreds of pixels (table S1).

2) Different spatial resolutions among the five observations analyzed in this work may introduce a bias when the spectra are compared: in particular, the higher the resolution, the more sensitive would be the measurement of the finest detail, which could not be resolved in lower-resolution observations. To address this issue, we only compared average spectra coming from the whole area of interest, covered by tens or hundreds of pixels, which is spatially resolved for all observations.

3) Although the area of interest is covered by these observations, the footprints of the spectrometer slit are not contiguous (fig. S2); thus, each point on the surface can be sampled in differing degrees of detail by the instrument, according to the position of the closest pixel footprint. This sampling heterogeneity introduces a further source of uncertainty. However, ~50% of the area of interest is covered by considering the pixel footprint only (fig. S2), and nearly 100% by considering the spatial extension of the point spread function of the instrument (fig. S3). Thus, the measured average signal should be representative, within the margin of error, of the whole area of interest, regardless of the extent of sampling of a particular area. This is confirmed by the same average signal of the test area shown in Fig. 3.

To evaluate the above-mentioned uncertainties, we simulated different spatial samplings and assessed the induced variability of the derived parameters. We used the following approaches: (i) random weights in the 0 to 2 range have been assigned to all pixels in the area of interest; (ii) a weighted average spectrum is calculated from the pixels with their assigned weights; (iii) the targeted spectral parameter is calculated from the average spectrum; (iv) the previous three points are repeated many times, starting from different random weights and thus obtaining a distribution of values of the targeted parameter; and (v) the error associated for each derived parameter is the SD of the corresponding distribution. The error bars of Figs. 2C and 4A are calculated in this way.Using this approach, we assigned a relative uncertainty of 100% for each pixel, simulating all the intermediate possibilities between the case in which a pixel is not detected and the case in which it is detected twice. This uncertainty propagates an error on the spectral parameter derived from the average spectrum, which is estimated by the approach discussed here.

4) In each observation, the total surface of the ice-rich wall can have a different projection of the corresponding area along the line of sight, according to the spacecraft position at the moment of observation. A different contribution between the area of the ice-rich wall and the area of outer regions (devoid of water ice), in the resulting average spectra, produces a fictitious variation of the spectral features. As an example of this effect, we observed an apparent smaller band area at 2.0 μm in L2, with respect to L1. To account for this issue, and to derive intrinsic spectral parameters of water ice in the ice-rich wall, a dedicated model has been implemented, as discussed in the "Spectral modeling" section.

Band area

The band area at 2.0 μm, reported in Figs. 2C and 4A, fig. S7, and table S2, is defined as

$$\int_a^b \left[1 - \frac{\text{reflectance}(\lambda)}{\text{continuum}(\lambda)}\right] d\lambda$$

where *a* and *b* are the edges of the bands: 1.83 to 2.24 μm. The continuum used to characterize the bands is calculated with a linear fit between *a* and *b*. The band area as defined above is expressed in micrometers. Error bars are estimated as discussed above.

Spectral modeling

The measured signal inside the region of interest defined in the main text is the sum of the radiance coming from the illuminated outer region (without ice) (OR) (Eq. 1) and the one coming from the ice-rich wall

(IRW) in shadow, but illuminated by the light reflected by the crater itself (Eq. 2). The nearly vertical wall in shadow is illuminated from all directions within the solid angle subtended by the crater as seen by the wall (~π steradians). To model the light scattered from the crater floor toward the shadowed wall, and the secondary scattered light from the latter toward the detector, we take into account the bi-hemispherical reflectance (*21*). Higher orders of scattering are assumed to be negligible.

The regolith of the ice-rich wall (Eq. 2) is modeled by an aerial mixture of water ice (WI) [optical constants by Warren (*22*), Mastrapa *et al.* (*23*), and Clark *et al.* (*24*)] and Ceres' average terrain (CAT) with optical properties as defined by Ciarniello *et al.* (*25*).

Using spectral modeling, we derived grain size of water ice of the order of 100 μm for all observations. This value is thus kept fixed in the fitting procedure discussed here.

$$\mathrm{Rad_{OR}} = J \times r_{\mathrm{R\_OR}} \times f \quad (1)$$

where $\mathrm{Rad_{OR}}$ is the radiance of the outer regions; J is the solar irradiance; $r_{\mathrm{R\_OR}}$ is the bidirectional reflectance (*21*) of Ceres' average terrain, with photometric parameters as defined by Ciarniello *et al.* (*25*), and viewing geometry by shape model analysis and spacecraft position at the moment of the observations (table S1); and $f = (1 + b^*(\lambda - \lambda_0) + c^*(\lambda - \lambda_0)^4)$ is the correction factor for the continuum slope, with b and c being constants derived in the fitting procedure, and λ_0 = 3.0 μm. This term accounts for the variation of the continuum slope due to spurious instrumental effects in correspondence with spatial signal contrast, such as shadowed regions. A similar approach is discussed by Ciarniello *et al.* (*19*). The models performed with and without this correction factor are shown in fig. S4.

$$\mathrm{Rad_{IRW}} = J \times (r_{\mathrm{s\_CAT}} <\mu_0>/\pi)/2 \times [r_{\mathrm{s\_WI}} p_{\mathrm{WI}} + r_{\mathrm{s\_CAT}}(1 - p_{\mathrm{WI}})] \quad (2)$$

where $\mathrm{Rad_{IRW}}$ is the radiance of the ice-rich wall; $r_{\mathrm{s\_CAT}}$ is the bi-hemispherical reflectance (*21*) of Ceres' average terrain; $<\mu_0>$ is the average incidence angle cosine on the crater at the time of the observation, derived by shape model analysis; ($r_{\mathrm{s\_CAT}} <\mu_0>/\pi$) represents the reflectance of a Lambertian surface, with Lambert albedo equal to $r_{\mathrm{s\_CAT}}$ (*20*); the factor 2 in the denominator accounts for the fact that one-half of the whole solid angle seen by the ice-rich wall is covered by the crater itself; $r_{\mathrm{s\_WI}}$ is the bi-hemispherical reflectance (*21*) of water ice; and p_{WI} is the cross section of water ice as a fraction of the total projected area of the ice-rich wall (in the main text, we refer to this quantity as water ice abundance)

$$\mathrm{Refl_{average}} = [\mathrm{Rad_{IRW}} \times p_{\mathrm{IRW}} + \mathrm{Rad_{OR}} \times p_{\mathrm{OR}}]/J \quad (3)$$

where $\mathrm{Refl_{average}}$ is the average reflectance; p_{IRW} is the cross section of the ice-rich wall as a fraction of the total projected area of interest; and $p_{\mathrm{OR}} = (1 - p_{\mathrm{IRW}})$ is the cross section of the outer regions as a fraction of the total projected area of interest.

Using a least-square optimization algorithm, we performed a model of $\mathrm{Refl_{average}}$ (Eq. 3) by fitting the measured reflectance, similar to that of Raponi *et al.* (*20*). Photometric correction of measured data is not required, because photometric parameters are included in the model as specified above.

As a result, we retrieved p_{IRW} and p_{WI} unambiguously. Spectral modeling was performed in the 1.15- to 3.55-μm interval to avoid the spectral range affected by thermal emission. Models are shown in fig. S5.

SUPPLEMENTARY MATERIALS

Supplementary material for this article is available at http://advances.sciencemag.org/cgi/content/full/4/3/eaao3757/DC1

fig. S1. Geological context.
fig. S2. Footprints of the VIR data visualized over the Framing Camera image mosaic.
fig. S3. Point spread function of the VIR instrument as derived from star observations.
fig. S4. Model of the average spectrum as a sum of outer region signal and ice-rich wall signal.
fig. S5. Modeled spectra with different abundances (left) and grain size (right).
fig. S6. Modeled best fits (red lines) of the five average spectra (black lines).
fig. S7. Model assuming constant water ice.
fig. S8. Water ice abundance of the ice-rich wall as a function of average solar flux.
fig. S9. Water vapor flux modeled.
table S1. Viewing geometry of the five observations.
table S2. Parameters and their errors retrieved in the best-fitting procedures as described in Materials and Methods.

REFERENCES AND NOTES

1. C. T. Russell, C. A. Raymond, E. Ammannito, D. L. Buczkowski, M. C. De Sanctis, H. Hiesinger, R. Jaumann, A. S. Konopliv, H. Y. McSween, A. Nathues, R. S. Park, C. M. Pieters, T. H. Prettyman, T. B. McCord, L. A. McFadden, S. Mottola, M. T. Zuber, S. P. Joy, C. Polanskey, M. D. Rayman, J. C. Castillo-Rogez, P. J. Chi, J. P. Combe, A. Ermakov, R. R. Fu, M. Hoffmann, Y. D. Jia, S. D. King, D. J. Lawrence, J.-Y. Li, S. Marchi, F. Preusker, T. Roatsch, O. Ruesch, P. Schenk, M. N. Villarreal, N. Yamashita, Dawn arrives at Ceres: Exploration of a small volatile-rich world. *Science* **353**, 1008–1010 (2016).
2. T. B. McCord, J. C. Castillo-Rogez, A. Rivkin, Ceres: Its origin, evolution and structure and *Dawn's* potential contribution. *Space Sci. Rev.* **163**, 63–76 (2011).
3. M. C. De Sanctis, E. Ammannito, A. Raponi, S. Marchi, T. B. McCord, H. Y. McSween, F. Capaccioni, M. T. Capria, F. G. Carrozzo, M. Ciarniello, A. Longobardo, F. Tosi, S. Fonte, M. Formisano, A. Frigeri, M. Giardino, G. Magni, E. Palomba, D. Turrini, F. Zambon, J.-P. Combe, W. Feldman, R. Jaumann, L. A. McFadden, C. M. Pieters, T. Prettyman, M. Toplis, C. A. Raymond, C. T. Russell, Ammoniated phyllosilicates with a likely outer Solar System origin on (1) Ceres. *Nature* **528**, 241–244 (2015).
4. T. H. Prettyman, N. Yamashita, M. J. Toplis, H. Y. McSween, N. Schörghofer, S. Marchi, W. C. Feldman, J. Castillo-Rogez, O. Forni, D. J. Lawrence, E. Ammannito, B. L. Ehlmann, H. G. Sizemore, S. P. Joy, C. A. Polanskey, M. D. Rayman, C. A. Raymond, C. T. Russell, Extensive water ice within Ceres' aqueously altered regolith: Evidence from nuclear spectroscopy. *Science* **355**, 55–59 (2017).
5. J.-P. Combe, T. B. McCord, F. Tosi, E. Ammannito, F. G. Carrozzo, M. C. De Sanctis, A. Raponi, S. Byrne, M. E. Landis, K. H. G. Hughson, C. A. Raymond, C. T. Russell, Detection of local H_2O exposed at the surface of Ceres. *Science* **353**, aaf3010 (2016).
6. T. Platz, A. Nathues, N. Schorghofer, F. Preusker, E. Mazarico, S. E. Schröder, S. Byrne, T. Kneissl, N. Schmedemann, J.-P. Combe, M. Schäfer, G. S. Thangjam, M. Hoffmann, P. Gutierrez-Marques, M. E. Landis, W. Dietrich, J. Ripken, K.-D. Matz, C. T. Russell, Surface water-ice deposits in the northern shadowed regions of Ceres. *Nat. Astron.* **1**, 0007 (2016).
7. M. C. De Sanctis, A. Coradini, E. Ammannito, G. Filacchione, M. T. Capria, S. Fonte, G. Magni, A. Barbis, A. Bini, M. Dami, I. Ficai-Veltroni, G. Preti; VIR Team, The VIR spectrometer. *Space Sci. Rev.* **163**, 329–369 (2011).
8. B. E. Schmidt, K. H. G. Hughson, H. T. Chilton, J. E. C. Scully, T. Platz, A. Nathues, H. Sizemore, M. T. Bland, S. Byrne, S. Marchi, D. P. O'Brien, N. Schorghofer, H. Hiesinger, R. Jaumann, J. H. Pasckert, J. D. Lawrence, D. Buzckowski, J. C. Castillo-Rogez, M. V. Sykes, P. M. Schenk, M.-C. DeSanctis, G. Mitri, M. Formisano, J.-Y. Li, V. Reddy, L. LeCorre, C. T. Russell, C. A. Raymond, Geomorphological evidence for ground ice on dwarf planet Ceres. *Nat. Geosci.* **10**, 338–343 (2017).
9. M. C. De Sanctis, A. Raponi, E. Ammannito, M. Ciarniello, M. J. Toplis, H. Y. McSween, J. C. Castillo-Rogez, B. L. Ehlmann, F. G. Carrozzo, S. Marchi, F. Tosi, F. Zambon, F. Capaccioni, M. T. Capria, S. Fonte, M. Formisano, A. Frigeri, M. Giardino, A. Longobardo, G. Magni, E. Palomba, L. A. McFadden, C. M. Pieters, R. Jaumann, P. Schenk, R. Mugnuolo, C. A. Raymond, C. T. Russell, Bright carbonate deposits as evidence of aqueous alteration on (1) Ceres. *Nature* **536**, 54–57 (2016).
10. O. Ruesch, T. Platz, P. Schenk, L. A. McFadden, J. C. Castillo-Rogez, L. C. Quick, S. Byrne, F. Preusker, D. P. O'Brien, N. Schmedemann, D. A. Williams, J.-Y. Li, M. T. Bland, H. Hiesinger, T. Kneissl, A. Neesemann, M. Schaefer, J. H. Pasckert, B. E. Schmidt, D. L. Buczkowski, M. V. Sykes, A. Nathues, T. Roatsch, M. Hoffmann, C. A. Raymond, C. T. Russell, Cryovolcanism on Ceres. *Science* **353**, aaf4286 (2016).
11. R. R. Fu, A. I. Ermakov, S. Marchi, J. C. Castillo-Rogez, C. A. Raymond, B. H. Hager, M. T. Zuber, S. D. King, M. T. Bland, M. C. De Sanctis, F. Preusker, R. S. Park, C. T. Russell, The interior structure of Ceres as revealed by surface topography. *Earth Planet. Sci. Lett.* **476**, 153–164 (2017).
12. M. Küppers, L. O'Rourke, D. Bockelée-Morvan, V. Zakharov, S. Lee, P. von Allmen, B. Carry, D. Teyssier, A. Marston, T. Müller, J. Crovisier, M. A. Barucci, R. Moreno, Localized sources of water vapour on the dwarf planet (1) Ceres. *Nature* **505**, 525–527 (2014).

13. M. F. A'Hearn, P. D. Feldman, Water vaporization on Ceres. *Icarus* **98**, 54–60 (1992).
14. M. N. Villarreal, C. T. Russell, J. G. Luhmann, W. T. Thompson, T. H. Prettyman, M. F. A'Hearn, M. Küppers, L. O'Rourke, C. A. Raymond, The dependence of the cerean exosphere on solar energetic particle events. *Astrophys. J. Lett.* **838**, L8 (2017).
15. M. C. De Sanctis, J. Lasue, M. T. Capria, G. Magni, D. Turrini, A. Coradini, Shape and obliquity effects on the thermal evolution of the Rosetta target 67P/Churyumov-Gerasimenko cometary nucleus. *Icarus* **207**, 341–358 (2010).
16. M. Formisano, M. C. De Sanctis, G. Magni, C. Federico, M. T. Capria, Ceres water regime: Surface temperature, water sublimation and transient exo(atmo)sphere. *Mon. Not. R. Astron. Soc.* **455**, 1892–1904 (2016).
17. M. C. De Sanctis, F. Capaccioni, M. Ciarniello, G. Filacchione, M. Formisano, S. Mottola, A. Raponi, F. Tosi, D. Bockelée-Morvan, S. Erard, C. Leyrat, B. Schmitt, E. Ammannito, G. Arnold, M. A. Barucci, M. Combi, M. T. Capria, P. Cerroni, W.-H. Ip, E. Kuehrt, T. B. McCord, E. Palomba, P. Beck, E. Quirico; The VIRTIS Team, The diurnal cycle of water ice on comet 67P/Churyumov–Gerasimenko. *Nature* **525**, 500–503 (2015).
18. G. Filacchione, M. C. De Sanctis, F. Capaccioni, A. Raponi, F. Tosi, M. Ciarniello, P. Cerroni, G. Piccioni, M. T. Capria, E. Palomba, G. Bellucci, S. Erard, D. Bockelee-Morvan, C. Leyrat, G. Arnold, M. A. Barucci, M. Fulchignoni, B. Schmitt, E. Quirico, R. Jaumann, K. Stephan, A. Longobardo, V. Mennella, A. Migliorini, E. Ammannito, J. Benkhoff, J. P. Bibring, A. Blanco, M. I. Blecka, R. Carlson, U. Carsenty, L. Colangeli, M. Combes, M. Combi, J. Crovisier, P. Drossart, T. Encrenaz, C. Federico, U. Fink, S. Fonti, W. H. Ip, P. Irwin, E. Kuehrt, Y. Langevin, G. Magni, T. McCord, L. Moroz, S. Mottola, V. Orofino, U. Schade, F. Taylor, D. Tiphene, G. P. Tozzi, P. Beck, N. Biver, L. Bonal, J-Ph. Combe, D. Despan, E. Flamini, M. Formisano, S. Fornasier, A. Frigeri, D. Grassi, M. S. Gudipati, D. Kappel, F. Mancarella, K. Markus, F. Merlin, R. Orosei, G. Rinaldi, M. Cartacci, A. Cicchetti, S. Giuppi, Y. Hello, F. Henry, S. Jacquinod, J. M. Reess, R. Noschese, R. Politi, G. Peter, Exposed water ice on the nucleus of comet 67P/Churyumov–Gerasimenko. *Nature* **529**, 368–372 (2016).
19. M. Ciarniello, A. Raponi, F. Capaccioni, G. Filacchione, F. Tosi, M. C. De Sanctis, D. Kappel, B. Rousseau, G. Arnold, M. T. Capria, M. A. Barucci, E. Quirico, A. Longobardo, E. Kuehrt, S. Mottola, S. Erard, D. Bockelée-Morvan, C. Leyrat, A. Migliorini, A. Zinzi, E. Palomba, B. Schmitt, G. Piccioni, P. Cerroni, W.-H. Ip, G. Rinaldi, M. Salatti, The global surface composition of 67P/Churyumov–Gerasimenko nucleus by *Rosetta*/VIRTIS. II) Diurnal and seasonal variability. *Mon. Not. R. Astron. Soc.* **462**, S443–S458 (2016).
20. A. Raponi, M. Ciarniello, F. Capaccioni, G. Filacchione, F. Tosi, M. C. De Sanctis, M. T. Capria, M. A. Barucci, A. Longobardo, E. Palomba, D. Kappel, G. Arnold, S. Mottola, B. Rousseau, E. Quirico, G. Rinaldi, S. Erard, D. Bockelee-Morvan, C. Leyrat, The temporal evolution of exposed water ice-rich areas on the surface of 67P/Churyumov–Gerasimenko: Spectral analysis. *Mon. Not. R. Astron. Soc.* **462**, S476–S490 (2016).
21. B. Hapke, *Theory of Reflectance and Emittance Spectroscopy* (Cambridge Univ. Press, ed. 2, 2012).
22. S. G. Warren, Optical constants of ice from the ultraviolet to the microwave. *Appl. Optics* **23**, 1206–1225 (1984).
23. R. M. Mastrapa, S. A. Sandford, T. L. Roush, D. P. Cruikshank, C. M. Dalle Ore, Optical constants of amorphous and crystalline H_2O-ice: 2.5–22 μm (4000–455 cm^{-1}) optical constants of H_2O-ice. *Astrophys. J.* **701**, 1347–1356 (2009).
24. R. N. Clark, D. P. Cruikshank, R. Jaumann, R. H. Brown, K. Stephan, C. Morea, D. Ore, K. E. Livo, N. Pearson, J. M. Curchin, T. M. Hoefen, B. J. Buratti, G. Filacchione, K. H. Baines, P. D. Nicholson, The surface composition of Iapetus: Mapping results from Cassini VIMS. *Icarus* **218**, 831–860 (2012).
25. M. Ciarniello, M. C. De Sanctis, E. Ammannito, A. Raponi, A. Longobardo, E. Palomba, F. G. Carrozzo, F. Tosi, J.-Y. Li, S. E. Schröder, F. Zambon, A. Frigeri, S. Fonte, M. Giardino, C. M. Pieters, C. A. Raymond, C. T. Russell, Spectrophotometric properties of dwarf planet Ceres from the VIR spectrometer on board the Dawn mission. *Astron. Astrophys.* **598**, A130 (2017).

Acknowledgments: We thank the Italian Space Agency (ASI), NASA, and the Deutsches Zentrum für Luft- und Raumfahrt for supporting this work. **Funding:** The VIR instrument was funded and coordinated by the ASI and built by Selex ES, with the scientific leadership of the Institute for Space Astrophysics and Planetology, Italian National Institute for Astrophysics, Italy, and it is operated by the Institute for Space Astrophysics and Planetology, Rome, Italy. **Author contributions:** A.R. wrote the manuscript, calibrated the data, and performed data analysis and interpretation; M.C.D.S. wrote the manuscript and contributed to data analysis and interpretation; A.F. performed geological analysis and contributed to interpretation; E.A. performed data calibration, instrument operations, and interpretation; M.C. contributed to spectral modeling and performed photometric analysis; M.F. performed thermal modeling; J.-P.C. contributed to data analysis; G.M. contributed to interpretation; F.T. provided geometry information; F.G.C. performed data calibration; S.F., M.G., S.P.J., C.A.P., and M.D.R. performed spacecraft and instrument operations; all authors helped with manuscript preparation. **Competing interests:** The authors declare that they have no competing interests. **Data and materials availability:** All data needed to evaluate the conclusions in the paper are present in the paper and/or the Supplementary Materials. Additional data related to this paper may be requested from the authors. Dawn data are archived in NASA's Planetary Data System; VIR spectral data may be obtained at http://sbn.psi.edu/pds/resource/dwncvir.html.

Submitted 13 July 2017
Accepted 23 January 2018
Published 14 March 2018
10.1126/sciadv.aao3757

Citation: A. Raponi, M. C. De Sanctis, A. Frigeri, E. Ammannito, M. Ciarniello, M. Formisano, J.-P. Combe, G. Magni, F. Tosi, F. G. Carrozzo, S. Fonte, M. Giardino, S. P. Joy, C. A. Polanskey, M. D. Rayman, F. Capaccioni, M. T. Capria, A. Longobardo, E. Palomba, F. Zambon, C. A. Raymond, C. T. Russell, Variations in the amount of water ice on Ceres' surface suggest a seasonal water cycle. *Sci. Adv.* **4**, eaao3757 (2018).